JGR Atmospheres

RESEARCH ARTICLE
10.1029/2024JD043157

Response of Mixed-Phase Cloud Microphysics to Aerosol Perturbations at the Contrasting Sites of Limassol, Cyprus, and Punta Arenas, Chile

Yun He[1,2,3], Patric Seifert[1], Cristofer Jimenez[1], Martin Radenz[1], Albert Ansmann[1], Johannes Bühl[1,4], Rodanthi-Elisavet Mamouri[5], and Boris Barja González[6]

[1]Leibniz Institute for Tropospheric Research (TROPOS), Leipzig, Germany, [2]School of Earth and Space Science and Technology, Wuhan University, Wuhan, China, [3]State Observatory for Atmospheric Remote Sensing, Wuhan, China, [4]Harz University of Applied Sciences, Wernigerode, Germany, [5]Eratosthenes Centre of Excellence, Limassol, Cyprus, [6]Atmospheric Research Laboratory, University of Magallanes, Punta Arenas, Chile

Key Points:

- Lidar-radar measurements quantified the link between ice-nucleating particle (INP) and ice crystal number concentrations (ICNC) in stratiform mixed-phase clouds
- For clouds in Limassol, ICNC agrees to INP concentration within an order of magnitude
- Current parameterizations may underestimate the marine-aerosol-related ice nucleating particle concentrations below −28 °C in the Southern-Hemisphere mid-latitudes' troposphere

Correspondence to:
Y. He,
heyun@whu.edu.cn

Citation:
He, Y., Seifert, P., Jimenez, C., Radenz, M., Ansmann, A., Bühl, J., et al. (2025). Response of mixed-phase cloud microphysics to aerosol perturbations at the contrasting sites of Limassol, Cyprus, and Punta Arenas, Chile. *Journal of Geophysical Research: Atmospheres*, *130*, e2024JD043157. https://doi.org/10.1029/2024JD043157

Received 16 DEC 2024
Accepted 16 SEP 2025

Abstract Ice crystal number concentrations (ICNC) of shallow stratiform mixed-phase clouds (MPCs) were contextualized with the ice nucleating particle concentrations (INPC) of the same airmass in which the cloud layers formed. Prerequisite are ground-based lidar and cloud radar observations from two sites with contrasting aerosol conditions: Limassol (34.67°N, 33.04°E), Cyprus, dominated by desert dust and continental aerosols, and Punta Arenas (53.13°S, 70.88°W), Chile, where marine aerosol and a so far unquantified fraction of aerosol from other sources prevails. For each MPC case, cloud-level INPC is derived from lidar observations of the cloud-free surroundings. The ICNC nucleated within the MPC is derived 180 m below the liquid-dominated cloud-top layer based on the synergetic observations from lidar and radar. At Limassol, both ICNC and INPC in dust-embedded MPC range from 0.05 to 3 L^{-1} and show good correlation. At similar temperatures, INPC derived in the free troposphere above Punta Arenas are at least one order of magnitude lower than at Limassol. In contrast, an agreement between ICNC (0.02–2 L^{-1}) and INPC (0.01–0.1 L^{-1}) at temperatures below −27 °C is not observed at Punta Arenas. Given the previously demonstrated reliability of the ICNC retrieval, we suggest that current parameterizations of free-tropospheric INPC at temperatures below −28 °C in the Southern Hemisphere midlatitudes might lack relevant components, due to scarcity of long-term in situ data sets of INPC at these conditions. Despite the identified discrepancies for Punta Arenas, our study highlights the crucial role of ice-nucleating particles in the primary ice formation of shallow stratiform MPCs.

Plain Language Summary This remote-sensing study provides further evidence that aerosol perturbations do significantly influence ice microphysics in shallow stratiform mixed-phase clouds (MPCs). MPCs occur at altitudes where temperatures range from 0 °C to −38 °C. They play an essential role in the global climate. Ice crystals in MPCs form via heterogeneous ice nucleation with the aid of ice-nucleating particles, which is one of the most important contributors to aerosol-cloud interactions, the primary source of uncertainty in climate models. We conducted lidar and radar observations to study shallow stratiform MPCs at two sites with contrasting aerosol conditions, that is, dusty and polluted Limassol, Cyprus, located in the Eastern Mediterranean, and the pristine site of Punta Arenas, Chile, in the Southern Ocean. We found a good agreement between INP number concentration (INPC) and ice crystal number concentrations (ICNC) at Limassol (both are 0.05–3 L^{-1}). Compared with Punta Arenas, MPCs over Limassol exhibit ten-fold (or even greater) higher INPC at comparable temperatures, generally resulting in an increase in ICNC by an order of magnitude. Suprisingly, at Punta Arenas a correlation between INPC and ICNC at temperatures below −27 °C is missing. This is probably caused by a potential underestimation of marine-aerosol-related INPC above Punta Arenas, which may be not well represented at temperatures below −28 °C.

1. Introduction

Mixed-phase clouds (MPCs), containing both supercooled liquid droplets and ice crystals, cover approximately one-thirds of the Earth's surface and play an essential role in the atmospheric radiation budget, precipitation formation, and cloud electrification (Mülmenstädt et al., 2015; Korolev et al., 2017; D. Zhang et al., 2018). In-cloud phase transitions from liquid (water droplet) to solid (ice crystal) cause significant changes in cloud effective radiative forcing, further modulating global climate (H. Zhang et al., 2023). Primary ice formation in mixed-phase clouds occurs at temperatures of 0 to −38 °C with the aid of aerosol acting as ice-nucleating particle

(INP), which is known as heterogeneous ice nucleation (He et al., 2021; Hoose & Möhler, 2012). Heterogeneous ice nucleation is rather complex, as the efficiency of INPs primarily depends on not only the environmental parameters (i.e., humidity and temperature), but also the aerosol properties themselves, including the aerosol type, particle size distribution (PSD), number concentration, and vertical distribution, which can vary significantly from region to region (Che et al., 2021; Kanji et al., 2017). These variations result in diverse changes in ice microphysics of MPCs, as observations (Radenz et al., 2021; Seifert et al., 2010; D. Zhang et al., 2018) as well as model simulations (Lee et al., 2024; Ma & Xie, 2013) suggested. On a global scale, the proportions of supercooled water and ice water at various temperatures observed by space-borne lidar are not well reproduced by the ECHAM6 (European Centre/Hamburg Version 6) and different versions of the CAM GCM (Community Atmosphere Model Global Climate Model) models (Komurcu et al., 2014), limiting our understanding of the effective radiative forcing resulting from aerosol-cloud interactions. This is partly due to regionally varying INP concentrations, which are influenced by aerosol concentration and aerosol-type-specific ice nucleation efficiency (Lohmann, 2017). Therefore, understanding the role of INP concentration (INPC) in ice microphysical properties of MPCs is of great importance to the assessment of global climate.

Over the very clean Southern Ocean (SO) (Foth et al., 2019), global climate models have been facing a difficulty in representing the cloud phase of MPC, which usually underestimate the liquid phase and result in incorrect cloud feedback (Bodas-Salcedo et al., 2016; Carlsen & David, 2022; Fiddes et al., 2022; Tan et al., 2016; X. Zhao et al., 2023). This finding has also been corroborated by a recent CMIP6 (Coupled Model Intercomparison Project Phase 6) evaluation, which reports that the underestimation of the liquid phase and the underestimation of cloud optical depth and effective radius together result in cloud radiative forcing that is comparable to observational data (L. Zhao et al., 2022). This is due to the inaccurate representation of the cloud-relevant properties of marine aerosols over the SO in the models (Twohy et al., 2021; Vergara-Temprado et al., 2018; Welti et al., 2020). In contrast, the Mediterranean Basin is much more polluted and strongly impacted by a mixture of several aerosol types, including marine aerosols in the boundary layer, long-range transported desert dust from North Africa and the Middle East, and trans-boundary continental aerosols from Europe (Abdelkader et al., 2015; Mamouri et al., 2016; Nisantzi et al., 2014). The regional variability in ice nucleating efficiency may significantly influence MPC properties (Ansmann et al., 2019). Data from campaigns in Punta Arenas (53.13°S, 70.88°W), Chile and Limassol (34.67°N, 33.04°E), Cyprus, which will be used within the herein presented study, provide a unique opportunity to study how different aerosol conditions in these two contrasting regions affect ice formation in MPCs.

Previous lidar-only studies have shown that the occurrence of heterogeneous ice formation at temperatures from −15 °C to −20 °C is much lower over Punta Arenas (<20%) compared to other sites on the globe (30 − 40% over Stellenbosch, South Africa and around 70% over Leipzig, Germany), where the atmosphere is in general prone to higher aerosol loadings (Kanitz et al., 2011). One of the important reasons that can explain the much fewer lidar-detected ice signatures over Punta Arenas is the ice water content being too low for lidar detection, as supported by a later study from Bühl et al. (2013), which found that lidar can only detect ice water content exceeding a threshold of approximately 10^{-6} $kg \cdot m^{-3}$. In addition, using ground-based lidar measurements, Radenz et al. (2021) took one step further toward a quantification of the INP conditions at Limassol and Punta Arenas. They have shown that dust particles and continental aerosols prevailing in Limassol are more efficient INPs than the predominant marine aerosols in Punta Arenas; moreover, the aerosol loading over Limassol is also much higher than that over Punta Arenas according to the averaged profiles of particle backscatter coefficient. As a result, compared to Limassol, Punta Arenas exhibits at least an order of magnitude lower INPCs and further 10 − 40% lower fractions of ice-containing clouds at temperatures ranging from −24 °C to −8 °C.

Based on a comparison of the radar reflectivity factor of the ice formed by MPCs over Limassol and Punta Arenas, Radenz et al. (2021) also provided a first indirect tracer that ice formation at Punta Arenas is not only less frequent but also quantitatively weaker than at Limassol. Recently, progress has been made in retrieving both, the microphysical properties of ice crystals formed in cirrus and MPCs from lidar-radar synergy, as well as the INP concentration in the aerosol layers surrounding the clouds from lidar observations (Ansmann et al., 2019). This study builds on the availability of new retrieval techniques and of the radar and lidar data sets from Limassol and Punta Arenas. Based on these prerequisites, it aims to derive a direct closure between the ice crystal number concentrations (ICNC) formed in MPCs and the INPC of the surrounding aerosol layers for the full range of possible cases identified from the data sets. The paper is organized as follows. Section 2 briefly describes the

instruments, data, and retrieval method. In Section 3, two case studies together with a statistical study (12 cases from Limassol and 8 cases from Punta Arenas) are presented. Lastly, a summary and conclusions are given in Section 4.

2. Data and Methods

2.1. Lidar-Radar Observations at Limassol and Punta Arenas

In this study, we utilize the observational data sets collected by the mobile Leipzig Aerosol and Cloud Remote Observations System (LACROS) from the Leibniz Institute for Tropospheric Research (Radenz et al., 2021). The instruments involved include a MIRA-35 35-GHz (wavelength: 8.5 mm) cloud radar and a portable Polly^{XT} multi-wavelength Raman polarization lidar, which are used to observe mixed-phase clouds (Baars et al., 2016; Engelmann et al., 2016). The MIRA-35 cloud radar is manufactured by METEK GmbH and can provide the profiles of Doppler spectra in two polarization channels, based on which radar reflectivity, linear depolarization ratio (LDR), Doppler velocity, and Doppler spectral width are derived (Görsdorf et al., 2015). Its raw data have a temporal resolution of 3 s and a vertical resolution of approximately 30 m. The Polly^{XT} Raman polarization lidar emits laser pulses at three wavelengths, that are, 355, 532, and 1,064 nm. The temporal and vertical resolution of the lidar raw data are 30 s and 7.5 m, respectively. LACROS, and correspondingly the same set of instrumentation, was deployed to both measurement sites of Limassol and Punta Arenas, which are addressed in the framework of this study (Radenz et al., 2021).

Observations in Limassol, Cyprus were conducted during the Cyprus Clouds, Aerosol, and Rain Experiment (CyCARE) campaign from October 2016 to March 2018 (Ansmann et al., 2019). The island of Cyprus is located in the eastern Mediterranean, where it is frequently influenced by a mixture of mineral dust from North Africa and Middle East, as well as by anthropogenic aerosols (e.g., urban haze and smoke) from surrounding continents. These complex aerosol sources play a vital role in affecting regional cloud formation and precipitation processes (Lelieveld et al., 2002). Observations in Punta Arenas, Chile were part of the Dynamics, Aerosol, Clouds, And Precipitation Observations in the Pristine Environment of the Southern Ocean (DACAPO-PESO) field campaign from November 2018 to November 2021 (Radenz et al., 2021). In Punta Arenas, only data collected before January 2020 were analyzed to exclude any potential influence of long-range transported smoke from Australian wildfires (Ohneiser et al., 2020; Yang et al., 2021). Punta Arenas is located at the southern tip of South America, the only continental landmass in the SO except Antarctica with prevailing westerly winds year-round. Its closest upwind landmasses are Australia and New Zealand (over 8,000 km away); thus, Punta Arenas is predominately affected by marine aerosols, with only a small fraction of less than 4% mass fraction of aerosols present in the background atmosphere (Foth et al., 2019; Gong et al., 2022; Radenz et al., 2021). Hereby, the contribution of continental aerosol to the free-tropospheric aerosol mix must be considered as preliminary, since no long-term statistics of free-tropospheric aerosol and INP concentrations for the Southern-Hemisphere midlatitudes do currently exist to the knowledge of the authors of this publication. The assumption of the 4% continental aerosol contribution to the free-tropospheric aerosol load is currently based on an airmass-apportionment study that was part of the study of Radenz et al. (2021).

The procedure for selecting well-defined stratiform supercooled cloud cases was initially introduced by Hogan et al. (2003) and Ansmann et al. (2008, 2009), and subsequently applied by Seifert et al. (2010), Bühl et al. (2016), Myagkov et al. (2016), Radenz et al. (2021), and Yi et al. (2024). This study employed a slightly modified and extended version of this selection scheme, as the properties of the surrounding aerosol are also considered. Figure 1 illustrates the approach to observe aerosol-cloud interaction in MPCs, focusing on the role of aerosols in ice formation. We focus on the typical shallow stratiform MPC composed of a thin (usually with thickness <500 m) supercooled liquid layer at top (blue) with ice virgae (red) below.

Note that MPC cases with another cloud situated above should be excluded, as potential seeder-feeder processes could affect the results. In such cases, if an ice crystal falling from an upper 'seeder' cloud is still surviving when reaching a lower-lying 'feeder' cloud, it may act as a nucleus for ice formation within the feeder cloud. This could obscure the intended focus on aerosol-induced heterogeneous ice nucleation (He et al., 2022; Li et al., 2024). To avoid this complication, we conservatively removed all seeder-feeder-related cases, despite the fact that the survival of a falling ice crystal depends on the vertical distance and humidity conditions between the clouds (Proske et al., 2021).

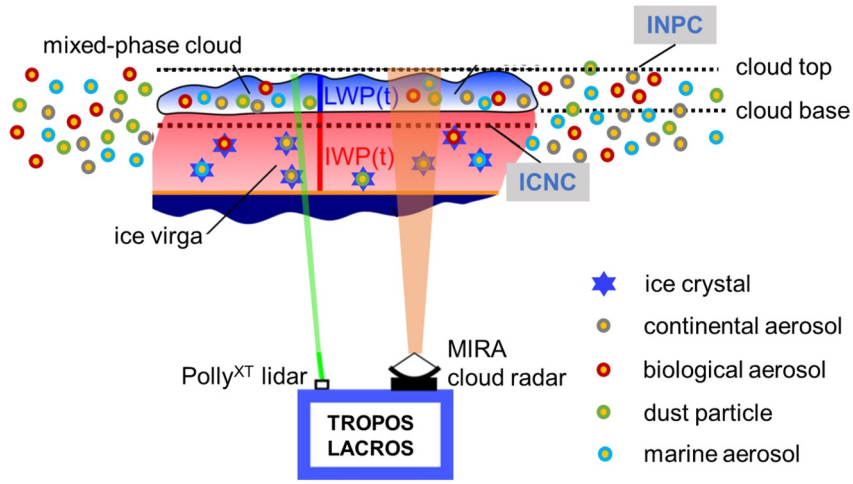

Figure 1. Schematic diagram of mixed-phase cloud observations with the combination of lidar (Polly^{XT}) and radar (Mira-35) based on (Bühl et al., 2016). INPC: ice-nucleating particle concentration at the cloud top. ICNC: ice crystal number concentration at 180 m below the base of the liquid-dominated layer.

The ice crystal number concentration is calculated based on the synergy of ground-based lidar and radar data using the LIRAS-ice (LIdar RAdar Synergy—retrieval of ice microphysical properties) approach from Bühl et al. (2019). We assume that the ICNC at a height of 180 m below the base of the liquid-dominated layer reflects the ICNC nucleated at the cloud top, indicating that neither riming nor aggregation processes, which may reduce the ICNC, have occurred yet. This notion was supported by previous studies of Bühl et al. (2016), Myagkov et al. (2016), and Radenz et al. (2021). The value of 180 m is employed according to our sensitivity analysis, which tested various heights below the cloud base. This height represents a trade-off: it should be neither too low nor too high. The main objective is to exclude the influence of the lidar signal from the liquid phase while also minimizing the impact of ice crystal evaporation or sublimation.

2.2. Retrieval of Ice Nucleating Particle Concentration

In order to enable the retrieval of INPC, a cloud-free period has to be available right before or after the occurrence of the MPC. The cloud top, being the coldest point of the cloud, is where heterogeneous ice nucleation most probably takes place; thus, the INPC at the height level of the cloud top is used in this study. Understanding the relationship between ICNC and INPC for each case will help us better constrain how aerosol perturbations influence MPC microphysics. It is priority to calculate INPC before cloud presence to avoid the potential impact of cloud scavenging. Once a cloud-free period is not available before cloud presence, INPC will then be calculated using the lidar measurements after cloud presence. In general, effects of scavenging of INP during cloud formation events that occurred before the air mass was probed by the remote sensing equipment cannot be evaluated, as cloud formation and evolution is a 4-dimensional process. For example, a cloud might have had already formed and dissolved again in an air mass that is found to be cloud-free above the lidar. During such an event, scavenging of INP from the cloud-level altitudes might occur. We evaluated two cases from the available data set during which INPC could be retrieved before and after a cloud event. Similar values were found, indicating that scavenging does not play a relevant role in these cases.

We employ the Polarization Lidar PHOtometer Networking (POLIPHON) method to determine the aerosol-type-dependent INPC from the aerosol properties in the cloud-free surroundings of the selected cloud cases (Mamouri & Ansmann, 2015, 2016). First, we retrieve the profiles of the 532-nm particle backscatter coefficient during a cloud-free period close to the time of cloud presence, preferably using the Raman method. When the Raman method is unavailable due to an insufficient signal-to-noise ratio, we instead apply the Fernald method (Fernald, 1984) as a secondary option. Then, the lidar-derived 532-nm particle backscatter coefficient is divided into dust and non-dust contributions (β_d and β_{nd}) based on the particle linear depolarization ratios δ_p of 0.31 and 0.05, respectively (Tesche et al., 2009). In Limassol, we consider the non-dust backscatter β_{nd} to be contributed by continental particle backscatter β_c; in some very warm cases (e.g., cloud top temperature (CTT) warmer than

Table 1
The INP Parameterizations (D-10(c), D-15(d), M-18(m), and T-13(b)) Applied for Different Types of Aerosols Are Given

Aerosol type	INP parameterization	Reference
Continental	$n_{\mathrm{INP,c}}(z) = a \cdot [273.16 - T(z)]^b \cdot n_{250,\mathrm{c,dry}}(z)^{[c(273.16-T(z))+d]}$ $a = 0.0000594, b = 3.33, c = 0.026, d = 0.0033$	DeMott et al. (2010)
Dust	$n_{\mathrm{INP,d}}(z) = f \cdot n_{250,\mathrm{d,dry}}(z)^{[a(273.16-T(z))+b]} \cdot \exp[c(273.16 - T(z)) + d]$ $a = 0, b = 1.25, c = 0.46, d = -11.6, f = 3.0$	DeMott et al. (2015)
Marine	$n_{\mathrm{INP,m}}(z) = s_{\mathrm{m,dry}} \cdot \exp[a(-273.16 + T(z)) + b]$ $a = -0.545, b = 1.0125$	McCluskey et al. (2018)
Biological	$n_{\mathrm{INP,b}}(z) = n_{250,\mathrm{b,dry}}(z)^{[a(273.16-T(z))+b]} \cdot \exp[c(273.16 - T(z)) + d]$ $a = -0.108, b = 3.8, c = 0, d = 4.605$	Tobo et al. (2013)

Note. $n_{250,\mathrm{i,dry}}$ denotes the number concentration of large particles with radius larger than 250 nm (unit in cm^{-3}) and $s_{\mathrm{i,dry}}$ denotes the surface area concentration (unit in $\mathrm{m}^2\mathrm{cm}^{-3}$). "i" represents each type of aerosols, which can be "c" for continental aerosol, "d" for dust aerosol, "m" for Marine aerosol, and "b" for biological aerosol, respectively. T denotes the temperature and can be given by the GDAS1 data. The corresponding references for each parameterization are also provided.

−12 °C), we will explore the possible presence of biological aerosols as INPs. In Punta Arenas, we assume the particle backscatter coefficient of background aerosols is primarily contributed by marine aerosols (96%) with a small fraction (4%) of that by continental aerosols, which is determined based on the particle depolarization ratio and air mass source estimates (Radenz et al., 2021). Then, the aerosol-type-specific particle backscatter coefficients are multiplied by lidar ratios of 45 sr (dust), 50 sr (continental aerosol), 20 sr (marine aerosol), and 70 sr (biological aerosol), to obtain the corresponding particle extinction coefficients (i.e., α_{d}, α_{c}, α_{m}, and α_{b}) (Floutsi et al., 2023; Müller et al., 2007; Shen et al., 2024). Note that continental aerosol is generally a mixture of different types of aerosols and its lidar ratio can be rather variable ranging from approximately 40–75 sr (Floutsi et al., 2023); thus, the largest uncertainty in the derived particle backscatter coefficient for continental aerosol can be up to 50%. The subscripts denote the aerosol type, which are "d" for dust, "m" for marine aerosol, "c" for continental aerosol, and "b" for biological aerosol, respectively.

By considering different conversion factors, the derived particle extinctions can be converted into the large-particle (with radius larger than 250 nm) number concentration $n_{250,\mathrm{i,dry}}$ and particle surface area concentration $s_{\mathrm{i,dry}}$ as follows:

$$n_{250,\mathrm{d,dry}}(z) = \mathrm{c}_{250,\mathrm{d}} \times \alpha_{\mathrm{d}}(z) \quad (1)$$

$$n_{250,\mathrm{c,dry}}(z) = \mathrm{c}_{290,\mathrm{c}} \times \alpha_{\mathrm{c}}(z) \quad (2)$$

$$s_{\mathrm{m,dry}}(z) = \mathrm{c}_{\mathrm{s,m}}/4 \times \alpha_{\mathrm{m}}(z) \quad (3)$$

$$n_{250,\mathrm{b,dry}}(z) = \mathrm{c}_{290,\mathrm{b}} \times \alpha_{\mathrm{b}}(z) \quad (4)$$

It should be noted that potential water-uptake by particle hygroscopicity has already been considered in the usage of conversion factors. For continental and biological aerosols, we use the conversion factors starting from "290 nm" rather than "250 nm"; for marine aerosols, we divide a factor of 4 for the conversion factor. In addition, dust is considered hydrophobic, thus particle water-uptake effect is not involved. The conversion factors are obtained from Mamouri and Ansmann (2016) as below, that is, $\mathrm{c}_{250,\mathrm{d}} = 0.18$ Mm cm^{-3}, $\mathrm{c}_{290,\mathrm{c}} = 0.10$ Mm cm^{-3}, $\mathrm{c}_{290,\mathrm{b}} = 0.09$ Mm cm^{-3}, and $\mathrm{c}_{\mathrm{s,m}}/4 = 0.63 \times 10^{-12}$ Mm m^2 cm^{-3}. These INP-relevant parameters serve as inputs for INP parameterizations to calculate the aerosol-type-specific INPC (He et al., 2023; Mamouri & Ansmann, 2016).

Considering only the immersion freezing process, we employ the INP parameterization D-15(d) (DeMott et al., 2015) for dust, D-10(c) (DeMott et al., 2010) for continental aerosol, M-18(m) (McCluskey et al., 2018) for marine aerosol, and T-13(b) (Tobo et al., 2013) for biological aerosol, as shown in Table 1. In addition, temperature and pressure data as input for the INP parameterization are provided by the GDAS1 (Global Data Assimilation System) data in both Limassol and Punta Arenas. Note that the D-10(c) and D-15(d)

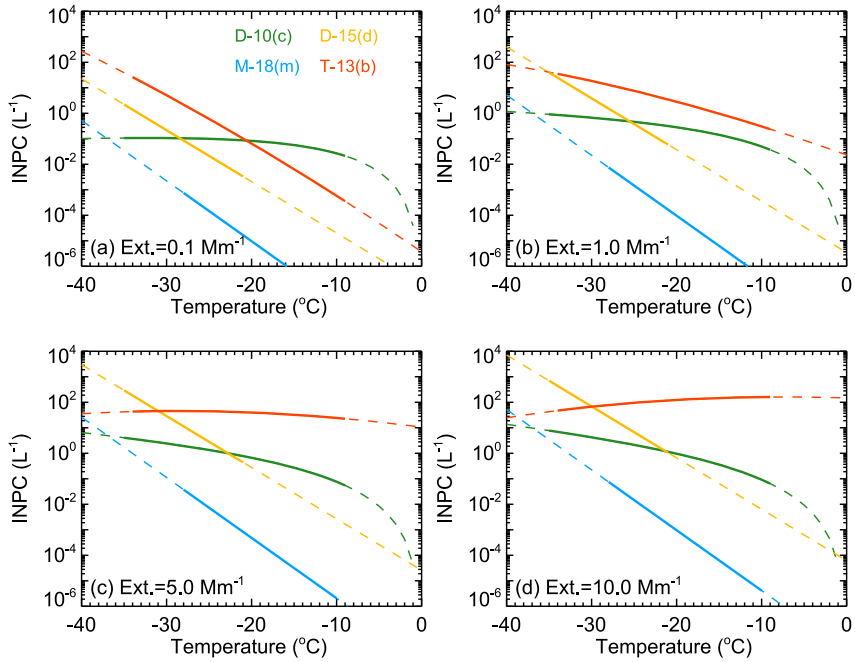

Figure 2. Performance of the four applied INP parameterizations for continental (D-10(c)), dust (D-15(d)), marine (M-18 (m)), and biological (T-13(b)) aerosols when giving four fixed particle extinction coefficients, (a) 0.1 Mm^{-1}, (b) 1 Mm^{-1}, (c) 5 Mm^{-1}, and (d) 10 Mm^{-1} (DeMott et al., 2010, 2015; McCluskey et al., 2018; Tobo et al., 2013). The dashed curves show the results at temperature ranging from 0 to −40 °C. The solid curves denote the results at respective valid temperature range for each parameterization.

parameterizations can be applied for the temperature ranges of −9 to −35 °C and −21 to −35 °C, respectively; whereas the M-18(m) and T-13(b) parameterizations are obtained by considering the data measured at temperatures from −10 to −28 °C and from −9 to −34 °C, respectively. We extend the application of D-15(d) to warmer temperatures up to −10 °C to analyze certain cases from Limassol with CTTs above −21 °C, as we consider D-15 (d) as the current optimal INP parameterization for mineral dust. Figure 2 shows the INPC-temperature relationships for the four INP parameterizations employed in this study, each representing a type of aerosol, at different particle extinction conditions. Here, we provide the results for each aerosol type from 0 to −40 °C (dashed curves) as well as at respective valid temperature range (solid curves). It is evidently seen that continental and biological aerosols can be efficient INPs at warmer conditions, for example, at temperatures above >−15 °C. Between −10 °C and −20 °C, for a given aerosol extinction, Figure 2 shows that continental aerosols can produce INPC values several times or even an order of magnitude higher compared to those from mineral dust, indicating that extending the valid temperature to these warmer conditions will not significantly affect the analysis in this work. In addition, marine aerosol that is mainly composed of sea salt is an inefficient INP type, providing at least 2–3 orders of magnitude less INPs than dust and continental aerosols; the only exception is that continental and marine aerosols generally contribute a similar level of INPC below −35 °C. Note that parameterization T-13(b) likely shows inappropriate results when particle extinction coefficient exceeds 5 Mm^{-1}, as the typical trend of INPC monotonously increasing with decreasing temperature no longer applies.

An estimation of the uncertainty in each retrieved parameter has been provided by Mamouri and Ansmann (2016), Ansmann et al. (2019), and Marinou et al. (2019). The uncertainty in the lidar-derived particle extinction and INP-relevant parameters, that is, $n_{250,i,dry}$ and $s_{i,dry}$, is estimated to be <30% and 30 − 50%, respectively. The current applied INP parameterizations contribute a majority of uncertainty to the calculated INPC; the uncertainty in the retrieved INPC is estimated to be a factor of 3 (Ansmann et al., 2019).

2.3. Retrieval of Ice Crystal Number Concentration

We can obtain the ice crystal number concentration within the ice virga region of MPCs by combining lidar and cloud radar observations using the method from Bühl et al. (2019), which was introduced as the LIRAS-ice

analysis scheme by Ansmann et al. (2025). The raw data of lidar and radar are integrated to a time resolution of 2 min and a vertical resolution of 7.5 m. Lidar observations provide 532-nm particle extinction of ice crystals and cloud radar measures 35-GHz reflectivity. Note that we use the particle extinction at 532 nm instead of 1064 nm for ICNC retrieval, as calibration of the backscatter coefficient retrieval is much easier at 532 nm due to the availability of sufficient molecular signal. Because of the different wavelength dependence of radar reflectivity Z and lidar-derived particle extinction E on crystal size, the Z-to-E ratio can be used to retrieve the median crystal maximum diameter and, subsequently, the ICNC values.

The retrieval method has been described in detail by Bühl et al. (2019). Thus, we provide only a brief overview of the ICNC calculation scheme here. First, we establish a lookup table with the following procedure. The PSD of ice crystals is assumed to follow the modified gamma distribution $N(D)$ from Ulbrich (1983), Sekelsky et al. (1999), and Hogan et al. (2003) expressed as follows:

$$N(D) = N_0 \left(\frac{D}{D_\mathrm{m}}\right)^{\mu} \exp\left[-(4+\mu)\frac{D}{D_\mathrm{m}}\right], \tag{5}$$

where D_m presents the median particle maximum diameter, μ is the shape parameter describing the tilt of the distribution (set to be 2), and D denotes the size (maximum diameter) of the ice crystal. The cloud radar reflectivity Z and lidar particle extinction coefficient E are then given, respectively, as

$$Z_\mathrm{lookup} = \int \frac{\mathrm{K}}{0.93} \cdot \left(\frac{6}{917\pi}\right)^2 N(D) m^2(D) / 0.001^6 \, \mathrm{d}D \tag{6}$$

$$E_\mathrm{lookup} = \int 2 \times N(D) A(D) \, \mathrm{d}D \tag{7}$$

where the dielectric constant $\mathrm{K} = 0.174$ for ice at 35 GHz, and the particle mass $m(D)$ and area $A(D)$ can be calculated according to the ice-shape-specific parameterization from Mitchell (1996). For a given D_m, we can obtain the only value of Z-to-E ratio, here expressed as $(Z/E)_\mathrm{lookup}$. This one-to-one relationship between $(Z/E)_\mathrm{lookup}$ and D_m is the lookup table, which is different for each ice crystal shape, as shown in Figure 3.

In practice, both the radar-measured reflectivity Z_meas and lidar-derived particle extinction E_meas can be obtained from the observations. The measured ratio $(Z/E)_\mathrm{meas}$ is then used to identify the best-fit $D_\mathrm{m,best}$ from the lookup table, which is subsequently put into the PSD $N(D)$ in Equation 5 to finally determine the ICNC N_meas as follows:

$$N_\mathrm{meas} = \int N_0 \left(\frac{D}{D_\mathrm{m,best}}\right)^{\mu} \exp\left[-(4+\mu)\frac{D}{D_\mathrm{m,best}}\right] \mathrm{d}D \tag{8}$$

Note that the aforementioned lidar particle backscatter coefficient for ice virga is derived using the Fernald method (Fernald, 1984) starting from a reference height at sub-cloud regions with a fixed lidar ratio of 20 sr. The reference values of the particle backscatter coefficient below the ice virga region are obtained from Raman retrievals during a cloud-free period nearby (as described in Section 2.2). The particle backscatter coefficient derived during a cloud-free period close to the time of cloud presence (also used for INPC calculations, as described in Section 2.2) is considered as the aerosol contribution to the total particle backscatter within the ice virga region and is thus removed before further calculations. The retrieved particle backscatter is then converted into particle extinction by multiplying by a larger lidar ratio of 32 sr to compensate for multiple scatterings by ice crystals (Seifert et al., 2007).

One prerequisite of the ICNC retrieval is the assignment of the observed ice crystals to a corresponding shape class. LIRAS-ice supports a series of possible shapes. As this study presumes primary ice formation in an environment that is saturated with respect to liquid water, we selected the shape class from Bühl et al. (2019), which corresponds best to the shapes found in laboratory studies (Bailey & Hallett, 2009) at the given cloud-top temperatures. As we presume that primary ice formation takes place, the shape was selected at different temperatures according to Bailey and Hallett (2009), as shown in Table 2. The parameterization for each ice shape can be found in Appendix A of Bühl et al. (2019). A comprehensive classification of all solid precipitation and their

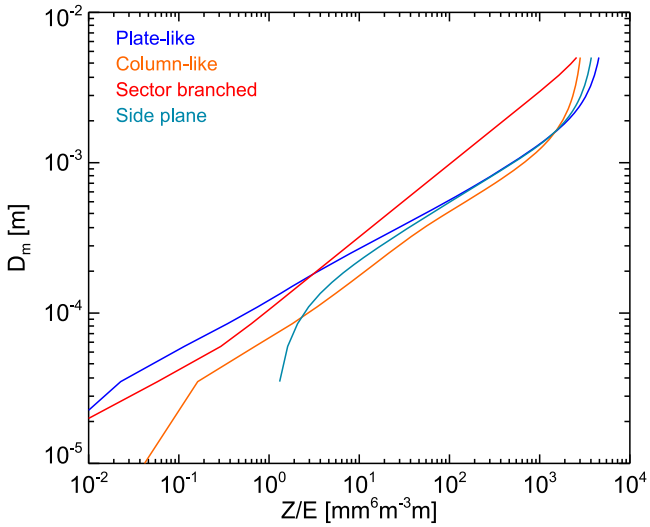

Figure 3. Relationship between the Z-to-E ratio and the median maximum diameter of ice crystal D_m for different types of typical ice crystal shapes. This is the lookup table for the LIRAS-ice ice crystal number concentrations retrieval.

microscopic photographs, including plate-like and sector-branched ice crystals can be found in Kikuchi et al. (2013). The overall uncertainty in the retrieved ICNC is estimated to be a factor of 2–5 (Ansmann et al., 2019).

3. Results

3.1. Limassol Case Study on 6 April 2017

Figures 4a–4c present a typical shallow stratiform MPC observed in Limassol from 1045 to 1130 UTC on 6 April 2017. The cloud was located at the top of a Saharan dust layer. As the cloud layer gradually descended, its top height was determined to be 4.8 km during the initial 10 minutes, with a CTT of −15.5 °C as estimated from the GDAS1 data. Correspondingly, the ice shape was assumed to be sector-branched for estimating the ICNC (Figure 4c). All cloud pixels with 532-nm extinction coefficient of >500 Mm^{-1} are considered to be liquid, and their corresponding ICNC values have been excluded. Note that the period of 1105–1130 UTC cannot be incorporated in calculating the case-average ICNC, since no sufficient ice signatures were detected at approximately 180 m below the liquid cloud base. Particle backscatter coefficient β_d and β_c, number concentration of particles larger than 250 nm (radius) $n_{250,d}$ and $n_{250,c}$, INPC $n_{INP,d}$ and $n_{INP,c}$ were retrieved during a cloud-free period (1200–1340 UTC, not shown) following the cloud presence. Here the non-dust component was all considered to be contributed by continental aerosols, as denoted by the subscript "c." Moreover, average ICNC of the ice virgae during the time frame from 1046 UTC to 1100 UTC is also presented.

At cloud heights (approximately 4–5 km), the particle backscatter coefficient from continental aerosol is slightly larger than that from dust. However, INPC contributed by continental aerosol is an order of magnitude larger than dust-related INPC at −15 °C. The total INPC is dominated by continental aerosols. This is because dust-related ice nucleation is only becomes increasingly efficient at temperatures below −15 °C (Kanji et al., 2017). The cloud-top INPC is 0.42 L^{-1}. The average ICNC at 180 m below the base of the liquid layer is approximately 0.16 L^{-1}, with a range of 0.05–0.48 L^{-1} by taking an uncertainty of a factor of 3 into consideration.

3.2. Punta Arenas Case Study on 28 November 2018

Figure 5 shows a long-lived, shallow stratiform MPC observed in Punta Arenas from 0120 to 0340 UTC on 28 November 2018, which has also been shown in Radenz et al. (2021). The cloud layer had a stable cloud top height at approximately 4.7 km, with a CTT of −14.8 °C as estimated by the GDAS1 data. Ice virgae are clearly seen below the liquid layer, particularly from 0150 UTC to 0230 UTC. Similar to the first case, the ice shape was assumed to be sector-branched for the ICNC estimate, and ICNC values have been excluded for pixels with 532-nm extinction coefficient of >500 Mm^{-1}. Particle backscatter coefficient β_c and β_m, number concentration of particles larger than 250 nm (radius) $n_{250,c}$, particle surface area concentration S_m, INPC $n_{INP,c}$ and $n_{INP,m}$ were retrieved during a cloud-free period (0350–0520 UTC) after the cloud presence. Here the marine aerosol is denoted by the subscript "m." Averaged ICNC of the ice virgae during the time frame from 0150 UTC to 0230 UTC is also shown.

Table 2
Assumption of Ice Crystal Shape at Different Temperatures Based on Bailey and Hallett (2009). The Shape-Dependent Parameterizations of Ice Crystals are Provided by Bühl et al. (2019)

Cloud top temperature (°C)	Ice shape from Bühl et al. (2019)
−8 to −12 °C	plate-like
−12 to −18 °C	sector branched
−18 to −35 °C	plate-like

This case shows a much cleaner atmospheric environment with a similar particle extinction level as observed in the Arctic (Ansmann et al., 2023; Garrett et al., 2010). At altitudes of 4–5 km, INPC levels for this Punta Arenas case (0.01–0.1 L^{-1}) are generally one order of magnitude lower than the Limassol case (0.1–1 L^{-1}), although the CTTs for the two cases are almost the same. This contrast is common according to our observations and will be discussed later in the statistical study subsection. Assuming that 4% of particle backscatter is contributed by continental aerosols, this small fraction still results in the dominance of continental aerosols in the total INP supply (four orders of magnitude more than marine aerosols). The total INPC (i.e., 96%

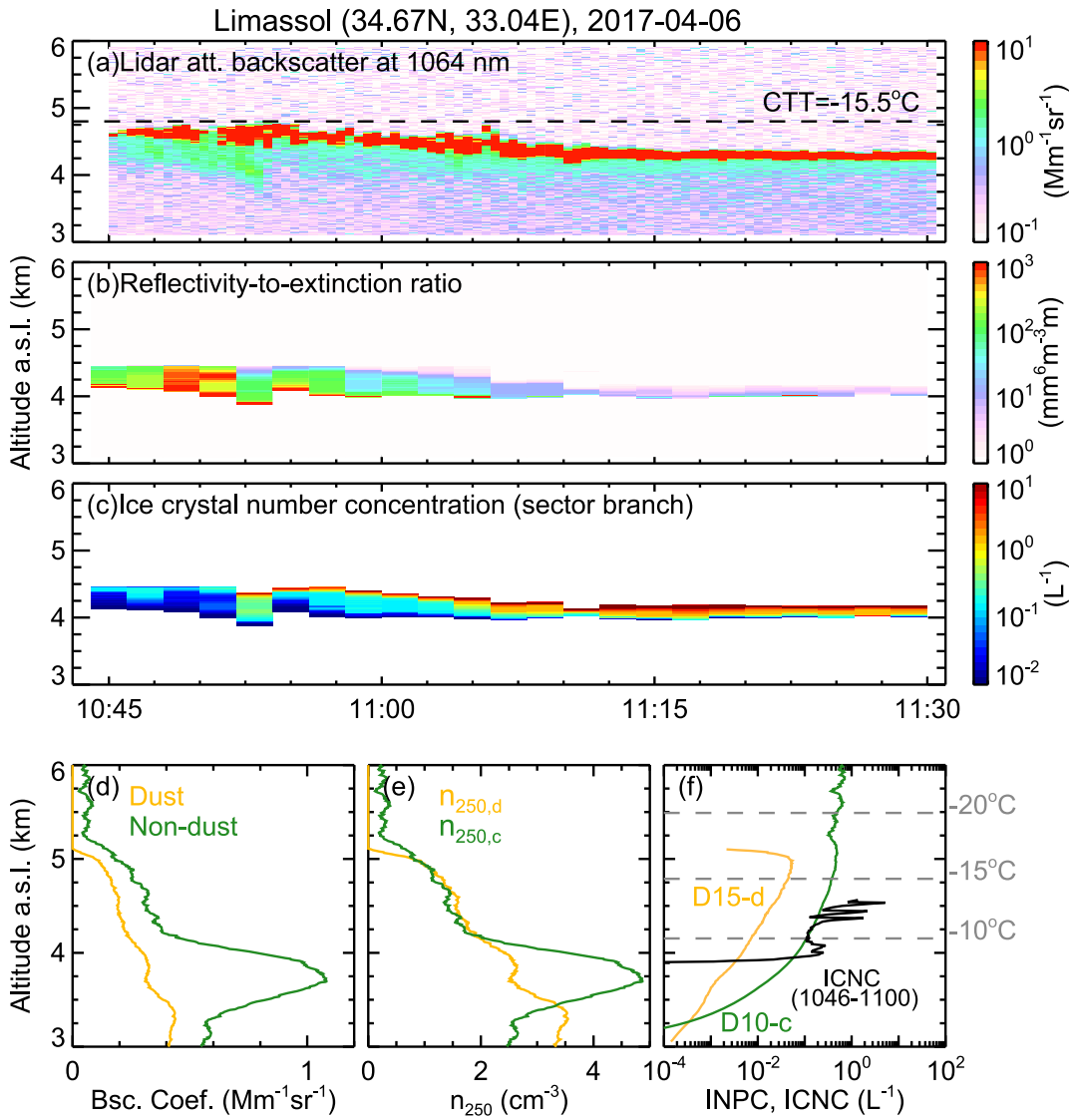

Figure 4. Lidar and radar observations of a mixed-phase cloud over Limassol during 1045–1130 UTC on 6 April 2017, including the time-altitude contour plots of the (a) lidar attenuated backscatter coefficient, (b) ratio of radar reflectivity to lidar-derived extinction, and (c) LIRAS-ice retrieval of ice crystal number concentration, and the profiles of the (d) aerosol backscatter coefficient (dust and non-dust), (e) n_{250} (dust and continental), and (f) ice nucleating particle concentrations (INPC) (dust and continental) and ice crystal number concentrations (ICNC). The ice crystals are assumed to have a sector branched shape based on the cloud top temperature of −15.5 °C. INPC is calculated during a cloud-free period of 1200–1340 UTC. ICNC is the mean value for a cloud-presence period of 1046–1100 UTC.

marine aerosols and 4% continental aerosols) is, on average, approximately 0.05 L^{-1} at the cloud top. Considering the retrieval uncertainty, the ICNC at 180 m below the base of the liquid-dominated layer is 0.01–0.09 L^{-1}, with a mean of 0.03 L^{-1}. The ICNC values agree well with INPC values within an order of magnitude, revealing that continental aerosols play a vital role in ice formation at the top of the MPC by serving as INPs.

3.3. Statistical Study

To verify the INPC-ICNC relationships suggested by means of the two cases, we further analyzed additional MPC cases at both sites (12 cases in Limassol and 8 cases in Punta Arenas) with the same method. The statistical results are shown in Figure 6.

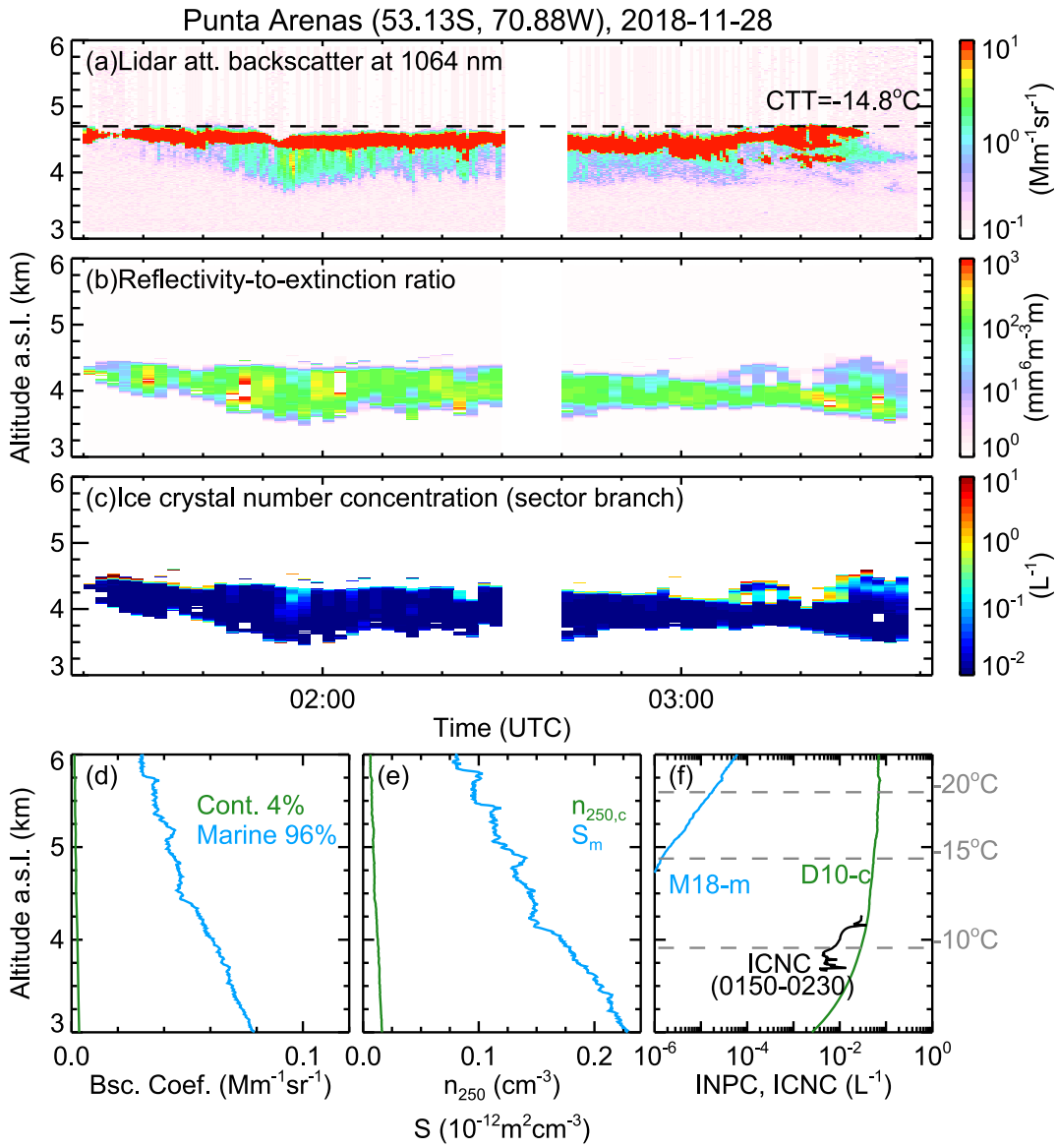

Figure 5. Lidar and radar observations of a mixed-phase cloud over Punta Arenas from 0120 to 0340 UTC on 28 November 2018, including the time-altitude contour plots of the (a) lidar attenuated backscatter coefficient, (b) ratio of radar reflectivity to lidar-derived extinction, and (c) LIRAS-ice retrieval of ice crystal number concentration, and the profiles of (d) aerosol backscatter coefficient (continental and marine), (e) n_{250} (continental) and S_m (marine), and (f) ice nucleating particle concentrations (INPC) (continental and marine) and ice crystal number concentrations (ICNC). The ice crystals are assumed to have a sector-branched shape based on the cloud top temperature of −14.8 °C. INPC is calculated during a cloud-free period of 0350–0520 UTC. ICNC is the mean value for the cloud-presence period from 0150 to 0230 UTC.

We placed the highest priority on selecting only those cases that provided ideal conditions for the INPC-to-ICNC closure study and that are representative for the expectable extreme environmental contrasts between Limassol (dust events) and Punta Arenas (unpolluted free troposphere). At Punta Arenas, only 8 cases were recorded due to the generally low temperatures, which rarely allow for the formation of stratiform liquid-topped MPCs above −15 °C. The relatively warm MPCs observed there are often linked to the aerosol-burden planetary boundary layer, as Radenz et al. (2021) point out. Also, convective conditions typically prevail in the lower troposphere, producing vertically extensive MPCs in which undesired secondary ice formation is highly probable. In addition, liquid-topped stratiform MPCs at lower temperatures are also frequently found to be surrounded by other cloud layers (increasing the likelihood of seeder-feeder events), influenced by orographic gravity waves, or composed of multiple embedded liquid layers Radenz et al. (2021). At Limassol, 12 cases were identified, involving the

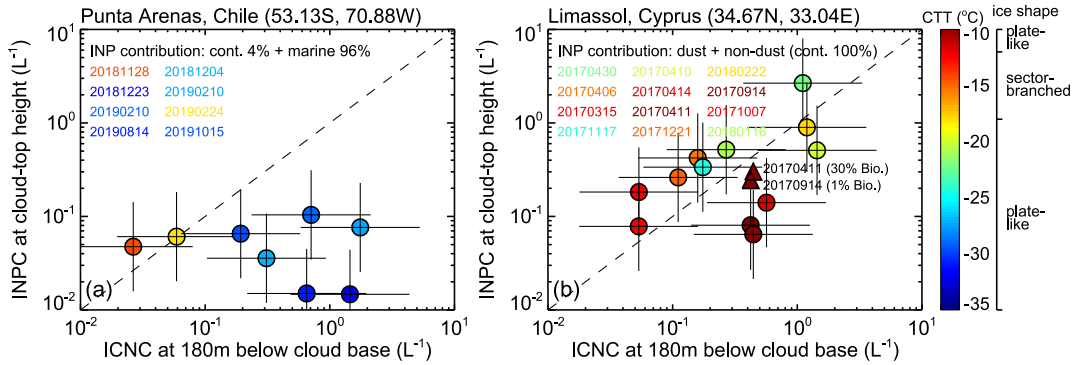

Figure 6. Statistical comparison of ice crystal number concentrations (ICNC) (180 m below liquid layer) with ice nucleating particle concentrations (INPC) (at cloud-top height) for mixed-phase cloud cases observed over (a) Punta Arenas and (b) Limassol. In Punta Arenas, INPCs are obtained by assuming 96% marine aerosols and 4% continental aerosols. In Limassol, INPCs are estimated by dust and continental aerosols. An uncertainty of a factor of 3 is given for both retrieved ICNC and INPC by the error bars. For two warmest Limassol cases, INPC values are adjusted by assuming 1% (14 September 2017) and 30% (11 April 2017) biological aerosols in total non-dust aerosols, as indicated by two triangles in (b).

primary INP type, that is, Saharan dust, which generally mixes with a fraction of continental aerosols (non-dust). It is worth noting that the co-located, well-defined occurrence of homogeneous, high-dust-load layers together with stratiform MPCs is relatively rare in the arid, sub-tropical climate of Cyprus.

As seen from Figure 6, the MPC cases from Punta Arenas show CTTs ranging from −14 to −31 °C, which are generally lower than those from Limassol (−10 to −25 °C). Using only lidar measurements, Kanitz et al. (2011) found that ice-containing clouds are rarely observed over Punta Arenas at CTTs above −20 °C, which was identified to be of strong contrast to observations from the research vessel Polarstern (three north-south ship-based campaigns), Stellenbosch (34°S, near Cape Town), South Africa, and Leipzig (51°N), Germany. After excluding cloud layers that are coupled to the aerosol-laden planetary boundary layer, Radenz et al. (2021) also reported that even by using a combination of lidar and radar hardly any ice signatures were detected in the free troposphere over Punta Arenas at temperatures above −15 °C. It is probably that Punta Arenas lacks of sufficient aerosols in the free troposphere to provide effective INPs at relatively higher temperatures (Foth et al., 2019; Radenz et al., 2021). Average INPC values at cloud top are estimated by considering dust and continental (100% of non-dust particles) aerosols in Limassol and marine (96% of non-dust particles) and continental (4% of non-dust particles) aerosols in Punta Arenas. Average ICNC at 180 m below the base of the liquid-dominated cloud-top layer is calculated to represent the ICNC nucleated at cloud top by assuming that riming, aggregation, secondary ice formation processes or sublimation of the crystals have not yet occurred.

In general, the INPC and ICNC values agree well within an order of magnitude on most occasions over Limassol if taking their uncertainties of a factor of 3 into consideration. For the two warmest MPC cases in Limassol, that is, on 11 April and 14 September 2017, the cloud-top temperatures of −10.2 °C and −9.8 °C are higher than the typical temperature of < -15 °C required for efficient dust-related ice nucleation (Kanji et al., 2017). Note that certain types of dust particles, such as K-feldspar, may contribute to ice nucleation at temperatures higher than −15 °C; however, it is still unclear whether K-feldspar is rich in Saharan dust (Atkinson et al., 2013; Boose et al., 2016; Kaufmann et al., 2016). This suggests that some effective INPs at warm temperatures might be neglected. To address the potential underestimation of INPCs, we consider some biological aerosols as effective INPs at warm temperatures (denoted by two triangles in Figure 6b), and find that the INPC in both cases increase to plausible levels when realistic fractions of biological INPs are presumed, revealing the strong relevance of INPs in the ice formation of MPCs. This may be a potential explanation for the more efficient heterogeneous ice nucleation for these two relatively warm cases. Additionally, we cannot rule out the possibility that the CTTs in these two cases are too warm for applying the INP parameterization D-15(d), which could potentially lead to an underestimation of dust-contributed INPC. However, it should be mentioned that a more solid conclusion needs further observations, such as in situ INP measurements. Both the INPC and ICNC values range from 0.05 to 3 L^{-1}. The statistically good closure between INPC and ICNC over Limassol is consistent with the case studies presented by Ansmann et al. (2019) at the same site. This indicates that the INP conditions, such as origin, type,

and concentration of the INPs, in Limassol are well characterized due to earlier extensive in situ measurement efforts, enabling the current INP parameterizations to well represent the INPC levels.

In contrast, a two-fold scenario is found for Punta Arenas. There, only the two relatively warm MPC cases on 28 November 2018 (CTT = −14.8 °C) and 24 February 2019 (CTT = −18.0 °C) fall near the one-to-one line, suggesting the good agreement between INPC and ICNC in this temperature range. For these two cases, ICNC range from 0.02 to 0.06 L^{-1}, whereas the INPC values range from 0.04 to 0.07 L^{-1}. These two measurements from Punta Arenas feature ICNC and IPNC which are approximately one order of magnitude lower than those observed at similar temperatures above Limassol.

For all lower-temperature cases, covering CTTs from −27 °C to −32 °C (see the blue points in Figure 6a), agreement between INPC and ICNC is not observed above Punta Arenas. The retrieved INPC at Punta Arenas are actually found to be rather independent of temperature, covering values between 0.01 and 0.1 L^{-1}. We consider the ICNC values of 0.02–0.2 L^{-1} in Punta Arenas to be reliable, since they have been validated in all cases in Limassol. It is reasonable to hypothesize that in Punta Arenas, the disagreement for the cases with CTTs below −27 °C is likely due to the underestimation of free-tropospheric INPC, specifically marine aerosol INPC values which were derived based on M-18(m) (McCluskey et al., 2018). It should be noted that there is a lack of INP parameterizations in representing the INP contribution of marine aerosols at temperatures below −28 °C. In McCluskey et al. (2018), all points used for the exponential fit of the relationship between temperature and nucleation site densities n_s (proportional to INPC) were measured at temperatures above −28 °C, which may lead to inapplicability under colder conditions. Furthermore, it has been found that at temperatures below −20 °C, the best-fit line in Figure 8 of McCluskey et al. (2018) might have a slightly steeper slope in logarithmic coordinates compared to the original one that they provided for a wide temperature range from −10 °C to −28 °C. This could cause a considerable factor to the underestimation of the calculated INPC for marine aerosols in cold cases. Moreover, we cannot completely exclude the possibility that, in the free troposphere over the SO, marine aerosols may contain other unknown materials that can serve as ice-nucleating sites at low temperatures which were so far not accounted for in the INP parameterizations. Nonetheless, we leave this as an open question, deserving further attention to help establish more applicative INP parameterizations for marine aerosols and to deepen our understanding of the type, origin, and concentration of INPs in the free troposphere over the SO.

Nevertheless, from Figure 6 it can be seen, that the previously reported large difference in INPCs between the two sites, as it was elaborated on already in Section 1, has also been observed. In Punta Arenas, INPCs for all cases range from 0.01 to 0.1 L^{-1}, generally an order of magnitude lower than the 0.05–3 L^{-1} observed in Limassol, further confirming that the presence of weakly INP-active marine aerosols (DeMott et al., 2016) in combination with the exceptionally low free-tropospheric aerosol load are responsible for a strongly limited INP reservoir. Although the INPC values for colder cases in Punta Arenas may be somewhat underestimated, the remaining two warmer cases (represented by the yellow and red points in Figure 6a), which have similar CTTs to those in Limassol, still exhibit INPCs an order of magnitude lower. This reveals that Punta Arenas has very few INPs available in the free troposphere, resulting in much fewer ice crystals forming in MPCs compared to the dusty and polluted atmosphere above Limassol. As a result, this INPC-ICNC comparison provides quantitative observational evidence that aerosol perturbations, through their role as INPs, significantly affect the ice microphysics in these shallow stratiform MPCs.

4. Summary and Conclusions

This study was dedicated to a closure between INPC and ICNC in shallow stratiform MPC. The underlying methodology is unique and has only recently been made available based on recent retrieval developments and the existence of harmonized long-term ground-based remote sensing data sets from contrasting key regions of aerosol-cloud interaction: pristine Southern Chile (Punta Arenas) in the SO region and the dust-laden Eastern Mediterranean (Limassol). Key instruments included a polarization Raman lidar and a vertically pointing 35-GHz cloud radar. The temporally and spatially high resolved data sets allowed for selecting those scenarios from the long-term data sets in which cloud layers were optimally defined by means of macrophysical and dynamically constrained liquid layer tops, the presence of ice virgae that formed therein, as well as the properties of the aerosol surrounding the cloud layers. The LIRAS-ice retrieval enabled the retrieval of ICNC from lidar-based extinction coefficients and radar-based reflectivity factors, incorporating in addition the preferred ice crystal habit, which significantly controls the retrieval due to its impact on mass-size relationships. Polarization lidar observations and

existing parameterizations were deployed to relate lidar-based aerosol extinction coefficients to INPCs, which were then put into context with the derived ICNC. Both retrievals go beyond what is currently possible to be achievable with space-borne remote sensing, where instruments lack the sensitivity for detecting small ice and aerosol concentrations, and retrievals below liquid cloud layers are prone to uncertainties caused by attenuation and coarse instrument resolution.

The methodology was illustrated by means of one case study from each site while in total 12 and 8 cases were analyzed for Limassol and Punta Arenas, respectively. The case studies together with the statistical results indicate that significant differences in cloud-top INPC influence the number concentration of pristine-nucleated ice crystals at the top of MPCs. In Limassol, abundant INPs originate from dust and continental aerosols, resulting in INPC values of 0.05–3 L^{-1}. This INP supply leads to similar ICNC values, ranging from 0.05 L^{-1} to 3 L^{-1}, indicating a statistically good closure between INPC and ICNC values. Therefore, it can be concluded that the INP conditions in Limassol, such as origin, type, and concentration, have been well characterized through extensive earlier measurements, enabling good representativeness in current INP parameterizations. In contrast, ICNC values in Punta Arenas are in general much lower, ranging from 0.02 L^{-1} to 2 L^{-1}. However, INPC values of 0.01–0.1 L^{-1} are derived for Punta Arenas by assuming that continental aerosols contribute 4% of the total aerosols, which dominate the INP supply. A good agreement between INPC and ICNC values is not observed in Punta Arenas for the 6 cloud cases with CTTs of below −27 °C, likely due to a potential underestimation of marine-aerosol-related free-tropospheric INPC for cold cases with CTTs from −27 °C to −32 °C. Currently, there is a lack of representative INP parameterizations for marine aerosols at temperatures below −28 °C, specifically with respect to the region of the SO. Even the M-18(m) parameterization (McCluskey et al., 2018) is based on measurements taken at temperatures warmer than −28 °C. In addition, at temperatures below −20 °C, the slope in Figure 8 of McCluskey et al. (2018) should be slightly steeper in logarithmic coordinates than that obtained over the entire temperature range from −10 °C to −28 °C, probably causing several-fold underestimations of derived marine aerosol INPC under cold conditions. Moreover, there is also a possibility that marine aerosols over the SO may contain other unknown materials capable of acting as ice-active sites, which are not incorporated in the current INP parameterizations. Nevertheless, we conclude that, compared to Limassol, the ten-fold (or greater) lower INPC in Punta Arenas quantitatively results in a corresponding reduction in ICNC by an order of magnitude.

In the future, it is planned to incorporate observations from Punta Arenas after January 2020, when long-range transported smoke from Australian wildfires was present frequently and widespread throughout the tropospheric column, especially at low temperatures (Ohneiser et al., 2020), which is another potential INP contributor (Ansmann et al., 2021). Furthermore, a similar study on aerosol-cloud interaction in MPCs will also be conducted in pristine Antarctica using remote sensing data collected at Neumayer Station III during the COALA (Continuous Observations of Aerosol-cLoud interAction) campaign in 2023 (Radenz et al., 2024) as well as in the polluted central Arctic during the MOSAiC (Multidisciplinary drifting Observatory for the Study of Arctic Climate) campaign in 2019–2020 (Ansmann et al., 2023). Moreover, it is anticipated that the lidar-radar combined detection from the EarthCARE (Earth Cloud Aerosol and Radiation Explorer) mission (Illingworth et al., 2015), launched in May 2024, will be involved in a global study. These extended studies will enhance our understanding on the role of different aerosols in modulating the microphysical properties of MPCs and thus the global climate system.

Data Availability Statement

The Polly^{XT} raw data are visible in the PollyNET database via the link: https://polly.tropos.de/ (PollyNET, 2024) and will become publicly available via the data portal of the European Aerosols, Clouds and Trace gases Research Infrastructure (ACTRIS) in the near future. The cloud radar raw data are provided by the ACTRIS Data Centre node for cloud profiling via the following links: https://hdl.handle.net/21.12132/2.a056a828a6b94d1f (Limassol) (Mamouri, 2021) and https://hdl.handle.net/21.12132/2.b6c194d7d33b448e (Punta Arenas) (CLU, 2021). The retrieved data for each mixed-phase cloud case, including the aerosol optical properties during cloud-free period, lidar particle extinctions during the presence of ice virga, and the derived ICNC data, can be obtained via the link https://doi.org/10.5281/zenodo.15645511 (He & Seifert, 2025).

Acknowledgments
YH acknowledges funding by National Natural Science Foundation of China (Grants 42575138 and 42005101), Hubei Provincial Natural Science Foundation of China (Grant 2023AFB617), and Chinese Scholarship Council (CSC) (Grant 202206275006). PS acknowledges funding by the Deutsche Forschungsgemeinschaft (DFG–German Research Foundation) project PICNICC (Grants SE2464/1-1 and KA4162/2-1) and by the Horizon Europe program project CleanCloud under Grant Agreement no. 101137639. MR acknowledges funding by European Union's Horizon 2020 research and innovation program project EXCELSIOR under grant agreement no. 857510.

References

Abdelkader, M., Metzger, S., Mamouri, R. E., Astitha, M., Barrie, L., Levin, Z., & Lelieveld, J. (2015). Dust–air pollution dynamics over the eastern Mediterranean. *Atmospheric Chemistry and Physics*, *15*(16), 9173–9189. https://doi.org/10.5194/acp-15-9173-2015

Ansmann, A., Jimenez, C., Roschke, J., Bühl, J., Ohneiser, K., Engelmann, R., et al. (2025). Impact of wildfire smoke on Arctic cirrus formation – Part 1: Analysis of MOSAiC 2019–2020 observations. *Atmospheric Chemistry and Physics*, *25*(9), 4847–4866. https://doi.org/10.5194/acp-25-4847-2025

Ansmann, A., Mamouri, R.-E., Bühl, J., Seifert, P., Engelmann, R., Hofer, J., et al. (2019). Ice-nucleating particle versus ice crystal number concentration in altocumulus and cirrus layers embedded in Saharan dust: A closure study. *Atmospheric Chemistry and Physics*, *19*(23), 15087–15115. https://doi.org/10.5194/acp-19-15087-2019

Ansmann, A., Ohneiser, K., Engelmann, R., Radenz, M., Griesche, H., Hofer, J., et al. (2023). Annual cycle of aerosol properties over the central Arctic during MOSAiC 2019–2020 – Light-extinction, CCN, and INP levels from the boundary layer to the tropopause. *Atmospheric Chemistry and Physics*, *23*(19), 12821–12849. https://doi.org/10.5194/acp-23-12821-2023

Ansmann, A., Ohneiser, K., Mamouri, R.-E., Knopf, D. A., Veselovskii, I., Baars, H., et al. (2021). Tropospheric and stratospheric wildfire smoke profiling with lidar: Mass, surface area, CCN, and INP retrieval. *Atmospheric Chemistry and Physics*, *21*(12), 9779–9807. https://doi.org/10.5194/acp-21-9779-2021

Ansmann, A., Tesche, M., Althausen, D., Müller, D., Seifert, P., Freudenthaler, V., et al. (2008). Influence of Saharan dust on cloud glaciation in southern Morocco during the Saharan mineral dust experiment. *Journal of Geophysical Research*, *113*(D4), D04210. https://doi.org/10.1029/2007JD008785

Ansmann, A., Tesche, M., Seifert, P., Althausen, D., Engelmann, R., Fruntke, J., et al. (2009). Evolution of the ice phase in tropical altocumulus: SAMUM lidar observations over Cape Verde. *Journal of Geophysical Research*, *114*(D17), D17208. https://doi.org/10.1029/2008JD011659

Atkinson, J. D., Murray, B. J., Woodhouse, M. T., Whale, T. F., Baustian, K. J., Carslaw, K. S., et al. (2013). The importance of feldspar for ice nucleation by mineral dust in mixed-phase clouds. *Nature*, *498*(7454), 355–358. https://doi.org/10.1038/nature12278

Baars, H., Kanitz, T., Engelmann, R., Althausen, D., Heese, B., Komppula, M., et al. (2016). An overview of the first decade of Polly^{NET}: An emerging network of automated Raman-polarization lidars for continuous aerosol profiling. *Atmospheric Chemistry and Physics*, *16*(8), 5111–5137. https://doi.org/10.5194/acp-16-5111-2016

Bailey, M. P., & Hallett, J. (2009). A comprehensive habit diagram for atmospheric ice crystals: Confirmation from the laboratory, AIRS II, and other field studies. *Journal of the Atmospheric Sciences*, *66*(9), 2888–2899. https://doi.org/10.1175/2009JAS2883.1

Bodas-Salcedo, A., Hill, P. G., Furtado, K., Williams, K. D., Field, P. R., Manners, J. C., et al. (2016). Large contribution of supercooled liquid clouds to the solar radiation budget of the Southern Ocean. *Journal of Climate*, *29*(11), 4213–4228. https://doi.org/10.1175/JCLI-D-15-0564.1

Boose, Y., Welti, A., Atkinson, J., Ramelli, F., Danielczok, A., Bingemer, H. G., et al. (2016). Heterogeneous ice nucleation on dust particles sourced from nine deserts worldwide – Part 1: Immersion freezing. *Atmospheric Chemistry and Physics*, *16*(23), 15075–15095. https://doi.org/10.5194/acp-16-15075-2016

Bühl, J., Ansmann, A., Seifert, P., Baars, H., & Engelmann, R. (2013). Toward a quantitative characterization of heterogeneous ice formation with lidar/radar: Comparison of calipso/cloudsat with ground-based observations. *Geophysical Research Letters*, *40*(16), 4404–4408. https://doi.org/10.1002/grl.50792

Bühl, J., Seifert, P., Myagkov, A., & Ansmann, A. (2016). Measuring ice- and liquid-water properties in mixed-phase cloud layers at the Leipzig cloudnet station. *Atmospheric Chemistry and Physics*, *16*(16), 10609–10620. https://doi.org/10.5194/acp-16-10609-2016

Bühl, J., Seifert, P., Radenz, M., Baars, H., & Ansmann, A. (2019). Ice crystal number concentration from lidar, cloud radar and radar wind profiler measurements. *Atmospheric Measurement Techniques*, *12*(12), 6601–6617. https://doi.org/10.5194/amt-12-6601-2019

Carlsen, T., & David, R. O. (2022). Spaceborne evidence that ice-nucleating particles influence high-latitude cloud phase. *Geophysical Research Letters*, *49*(14), e2022GL098041. https://doi.org/10.1029/2022GL098041

Che, Y., Zhang, J., Zhao, C., Fang, W., Xue, W., Yang, W., et al. (2021). A study on the characteristics of ice nucleating particles concentration and aerosols and their relationship in spring in Beijing. *Atmospheric Research*, *247*, 105196. https://doi.org/10.1016/j.atmosres.2020.105196

CLU. (2021). Custom collection of categorize, classification, drizzle, ice water content, and liquid water content data from Punta Arenas between 27 Nov 2018 and 31 Dec 2020 [Dataset]. *ACTRIS Cloud remote sensing data centre unit (CLU)*. Retrieved from https://hdl.handle.net/21.12132/2.b6c194d7d33b448e

DeMott, P. J., Hill, T. C. J., McCluskey, C. S., Prather, K. A., Collins, D. B., Sullivan, R. C., et al. (2016). Sea spray aerosol as a unique source of ice nucleating particles. *Proceedings of the National Academy of Sciences*, *113*(21), 5797–5803. https://doi.org/10.1073/pnas.1514034112

DeMott, P. J., Prenni, A. J., Liu, X., Kreidenweis, S. M., Petters, M. D., Twohy, C. H., et al. (2010). Predicting global atmospheric ice nuclei distributions and their impacts on climate. *Proceedings of the National Academy of Sciences*, *107*(25), 11217–11222. https://doi.org/10.1073/pnas.0910818107

DeMott, P. J., Prenni, A. J., McMeeking, G. R., Sullivan, R. C., Petters, M. D., Tobo, Y., et al. (2015). Integrating laboratory and field data to quantify the immersion freezing ice nucleation activity of mineral dust particles. *Atmospheric Chemistry and Physics*, *15*(1), 393–409. https://doi.org/10.5194/acp-15-393-2015

Engelmann, R., Kanitz, T., Baars, H., Heese, B., Althausen, D., Skupin, A., et al. (2016). The automated multiwavelength Raman polarization and water-vapor lidar Polly^{XT}: The neXT generation. *Atmospheric Measurement Techniques*, *9*(4), 1767–1784. https://doi.org/10.5194/amt-9-1767-2016

Fernald, F. G. (1984). Analysis of atmospheric lidar observations: Some comments. *Applied Optics*, *23*(5), 652–653. https://doi.org/10.1364/AO.23.000652

Fiddes, S. L., Protat, A., Mallet, M. D., Alexander, S. P., & Woodhouse, M. T. (2022). Southern Ocean cloud and shortwave radiation biases in a nudged climate model simulation: Does the model ever get it right? *Atmospheric Chemistry and Physics*, *22*(22), 14603–14630. https://doi.org/10.5194/acp-22-14603-2022

Floutsi, A. A., Baars, H., Engelmann, R., Althausen, D., Ansmann, A., Bohlmann, S., et al. (2023). DeLiAn – A growing collection of depolarization ratio, lidar ratio and Ångström exponent for different aerosol types and mixtures from ground-based lidar observations. *Atmospheric Measurement Techniques*, *16*(9), 2353–2379. https://doi.org/10.5194/amt-16-2353-2023

Foth, A., Kanitz, T., Engelmann, R., Baars, H., Radenz, M., Seifert, P., et al. (2019). Vertical aerosol distribution in the southern hemispheric midlatitudes as observed with lidar in Punta Arenas, Chile (53.2°S and 70.9°W), during ALPACA. *Atmospheric Chemistry and Physics*, *19*(9), 6217–6233. https://doi.org/10.5194/acp-19-6217-2019

Garrett, T. J., Zhao, C., & Novelli, P. C. (2010). Assessing the relative contributions of transport efficiency and scavenging to seasonal variability in Arctic aerosol. *Tellus B: Chemical and Physical Meteorology*, *62*(3), 190–196. https://doi.org/10.1111/j.1600-0889.2010.00453.x

Gong, X., Radenz, M., Wex, H., Seifert, P., Ataei, F., Henning, S., et al. (2022). Significant continental source of ice-nucleating particles at the tip of Chile's southernmost Patagonia region. *Atmospheric Chemistry and Physics*, *22*(16), 10505–10525. https://doi.org/10.5194/acp-22-10505-2022

Görsdorf, U., Lehmann, V., Bauer-Pfundstein, M., Peters, G., Vavriv, D., Vinogradov, V., & Volkov, V. (2015). A 35-GHz polarimetric doppler radar for long-term observations of cloud Parameters—description of system and data processing. *Journal of Atmospheric and Oceanic Technology*, *32*(4), 675–690. https://doi.org/10.1175/JTECH-D-14-00066.1

He, Y., & Seifert, P. (2025). Mixed-phase cloud cases from TROPOS lidar-radar observations over limassol and Punta Arenas [Dataset]. *Zenodo*. Retrieved from https://doi.org/10.5281/zenodo.15645511

He, Y., Yi, F., Liu, F., Yin, Z., Yi, Y., Zhou, J., et al. (2022). Natural seeder-feeder process originating from mixed-phase clouds observed with polarization lidar and radiosonde at a mid-latitude plain site. *Journal of Geophysical Research: Atmospheres*, *127*(5), e2021JD036094. https://doi.org/10.1029/2021JD036094

He, Y., Yi, F., Yi, Y., Liu, F., & Zhang, Y. (2021). Heterogeneous nucleation of midlevel cloud layer influenced by transported Asian dust over Wuhan (30.5°N, 114.4°E), China. *Journal of Geophysical Research: Atmospheres*, *126*(2), e2020JD033394. https://doi.org/10.1029/2020JD033394

He, Y., Yin, Z., Ansmann, A., Liu, F., Wang, L., Jing, D., & Shen, H. (2023). POLIPHON conversion factors for retrieving dust-related cloud condensation nuclei and ice-nucleating particle concentration profiles at oceanic sites. *Atmospheric Measurement Techniques*, *16*(7), 1951–1970. https://doi.org/10.5194/amt-16-1951-2023

Hogan, R. J., Francis, P. N., Flentje, H., Illingworth, A. J., Quante, M., & Pelon, J. (2003). Characteristics of mixed-phase clouds. I: Lidar, radar and aircraft observations from CLARE'98. *Quarterly Journal of the Royal Meteorological Society*, *129*(592), 2089–2116. https://doi.org/10.1256/rj.01.208

Hoose, C., & Möhler, O. (2012). Heterogeneous ice nucleation on atmospheric aerosols: A review of results from laboratory experiments. *Atmospheric Chemistry and Physics*, *12*(20), 9817–9854. https://doi.org/10.5194/acp-12-9817-2012

Illingworth, A. J., Barker, H. W., Beljaars, A., Ceccaldi, M., Chepfer, H., Clerbaux, N., et al. (2015). The EarthCARE satellite: The next step forward in global measurements of clouds, aerosols, precipitation, and radiation. *Bulletin of the American Meteorological Society*, *96*(8), 1311–1332. https://doi.org/10.1175/BAMS-D-12-00227.1

Kanitz, T., Seifert, P., Ansmann, A., Engelmann, R., Althausen, D., Casiccia, C., & Rohwer, E. G. (2011). Contrasting the impact of aerosols at northern and southern midlatitudes on heterogeneous ice formation. *Geophysical Research Letters*, *38*(17), L17802. https://doi.org/10.1029/2011GL048532

Kanji, Z. A., Ladino, L. A., Wex, H., Boose, Y., Burkert-Kohn, M., Cziczo, D. J., & Krämer, M. (2017). Overview of ice nucleating particles. *Meteorological Monographs*, *58*, 1.1–1.33. https://doi.org/10.1175/AMSMONOGRAPHS-D-16-0006.1

Kaufmann, L., Marcolli, C., Hofer, J., Pinti, V., Hoyle, C. R., & Peter, T. (2016). Ice nucleation efficiency of natural dust samples in the immersion mode. *Atmospheric Chemistry and Physics*, *16*(17), 11177–11206. https://doi.org/10.5194/acp-16-11177-2016

Kikuchi, K., Kameda, T., Higuchi, K., & Yamashita, A. (2013). A global classification of snow crystals, ice crystals, and solid precipitation based on observations from middle latitudes to polar regions. *Atmospheric Research*, *132–133*, 460–472. https://doi.org/10.1016/j.atmosres.2013.06.006

Komurcu, M., Storelvmo, T., Tan, I., Lohmann, U., Yun, Y., Penner, J. E., et al. (2014). Intercomparison of the cloud water phase among global climate models. *Journal of Geophysical Research: Atmospheres*, *119*(6), 3372–3400. https://doi.org/10.1002/2013JD021119

Korolev, A., McFarquhar, G., Field, P. R., Franklin, C., Lawson, P., Wang, Z., et al. (2017). Mixed-phase clouds: Progress and challenges. *Meteorological Monographs*, *58*, 5.1–5.50. https://doi.org/10.1175/AMSMONOGRAPHS-D-17-0001.1

Lee, J., Seifert, P., Hashino, T., Maahn, M., Senf, F., & Knoth, O. (2024). Simulations of the impact of cloud condensation nuclei and ice-nucleating particles perturbations on the microphysics and radar reflectivity factor of stratiform mixed-phase clouds. *Atmospheric Chemistry and Physics*, *24*(10), 5737–5756. https://doi.org/10.5194/acp-24-5737-2024

Lelieveld, J., Berresheim, H., Borrmann, S., Crutzen, P. J., Dentener, F. J., Fischer, H., et al. (2002). Global air pollution crossroads over the Mediterranean. *Science*, *298*(5594), 794–799. https://doi.org/10.1126/science.1075457

Li, D., Zhao, C., Yang, J., Liu, C., Wang, T., Chen, Y., et al. (2024). Seeding invigoration effect of ice-containing clouds on lower convective clouds during MeiYu season in 2020. *Atmospheric Research*, *301*, 107288. https://doi.org/10.1016/j.atmosres.2024.107288

Lohmann, U. (2017). Anthropogenic aerosol influences on mixed-phase clouds. *Current Climate Change Reports*, *3*(1), 32–44. https://doi.org/10.1007/s40641-017-0059-9

Ma, J., & Xie, S.-P. (2013). Regional patterns of sea surface temperature change: A source of uncertainty in future projections of precipitation and atmospheric circulation. *Journal of Climate*, *26*(8), 2482–2501. https://doi.org/10.1175/JCLI-D-12-00283.1

Mamouri, R.-E. (2021). Custom collection of categorize, classification, drizzle, ice water content, and liquid water content data from limassol between 19 Oct 2016 and 25 Mar 2018 [Dataset]. *ACTRIS Cloud remote sensing data centre unit (CLU)*. Retrieved from https://hdl.handle.net/21.12132/2.a056a828a6b94d1f

Mamouri, R.-E., & Ansmann, A. (2015). Estimated desert-dust ice nuclei profiles from polarization lidar: Methodology and case studies. *Atmospheric Chemistry and Physics*, *15*(6), 3463–3477. https://doi.org/10.5194/acp-15-3463-2015

Mamouri, R.-E., & Ansmann, A. (2016). Potential of polarization lidar to provide profiles of CCN- and INP-relevant aerosol parameters. *Atmospheric Chemistry and Physics*, *16*(9), 5905–5931. https://doi.org/10.5194/acp-16-5905-2016

Mamouri, R.-E., Ansmann, A., Nisantzi, A., Solomos, S., Kallos, G., & Hadjimitsis, D. G. (2016). Extreme dust storm over the eastern Mediterranean in September 2015: Satellite, lidar, and surface observations in the Cyprus region. *Atmospheric Chemistry and Physics*, *16*(21), 13711–13724. https://doi.org/10.5194/acp-16-13711-2016

Marinou, E., Tesche, M., Nenes, A., Ansmann, A., Schrod, J., Mamali, D., et al. (2019). Retrieval of ice-nucleating particle concentrations from lidar observations and comparison with UAV in situ measurements. *Atmospheric Chemistry and Physics*, *19*(17), 11315–11342. https://doi.org/10.5194/acp-19-11315-2019

McCluskey, C. S., Ovadnevaite, J., Rinaldi, M., Atkinson, J., Belosi, F., Ceburnis, D., et al. (2018). Marine and terrestrial organic ice-nucleating particles in pristine marine to continentally influenced Northeast Atlantic air masses. *Journal of Geophysical Research: Atmospheres*, *123*(11), 6196–6212. https://doi.org/10.1029/2017JD028033

Mitchell, D. L. (1996). Use of Mass- and area-dimensional power laws for determining precipitation particle terminal velocities. *Journal of the Atmospheric Sciences*, *53*(12), 1710–1723. https://doi.org/10.1175/1520-0469(1996)053⟨1710:UOMAAD⟩2.0.CO;2

Müller, D., Ansmann, A., Mattis, I., Tesche, M., Wandinger, U., Althausen, D., & Pisani, G. (2007). Aerosol-type-dependent lidar ratios observed with Raman lidar. *Journal of Geophysical Research*, *112*(D16), D16202. https://doi.org/10.1029/2006JD008292

Mülmenstädt, J., Sourdeval, O., Delanoë, J., & Quaas, J. (2015). Frequency of occurrence of rain from liquid-mixed-and ice-phase clouds derived from A-Train satellite retrievals. *Geophysical Research Letters*, *42*(15), 6502–6509. https://doi.org/10.1002/2015GL064604

Myagkov, A., Seifert, P., Wandinger, U., Bühl, J., & Engelmann, R. (2016). Relationship between temperature and apparent shape of pristine ice crystals derived from polarimetric cloud radar observations during the ACCEPT campaign. *Atmospheric Measurement Techniques*, *9*(8), 3739–3754. https://doi.org/10.5194/amt-9-3739-2016

Nisantzi, A., Mamouri, R. E., Ansmann, A., & Hadjimitsis, D. (2014). Injection of mineral dust into the free troposphere during fire events observed with polarization lidar at Limassol, Cyprus. *Atmospheric Chemistry and Physics*, *14*(22), 12155–12165. https://doi.org/10.5194/acp-14-12155-2014

Ohneiser, K., Ansmann, A., Baars, H., Seifert, P., Barja, B., Jimenez, C., et al. (2020). Smoke of extreme Australian bushfires observed in the stratosphere over Punta Arenas, Chile, in January 2020: Optical thickness, lidar ratios, and depolarization ratios at 355 and 532 nm. *Atmospheric Chemistry and Physics*, *20*(13), 8003–8015. https://doi.org/10.5194/acp-20-8003-2020

PollyNET. (2024). Worldwide observations with the portable Raman lidar systems (Polly) [Dataset]. Retrieved from https://polly.tropos.de/

Proske, U., Bessenbacher, V., Dedekind, Z., Lohmann, U., & Neubauer, D. (2021). How frequent is natural cloud seeding from ice cloud layers (<−35c) over Switzerland? *Atmospheric Chemistry and Physics*, *21*(6), 5195–5216. https://doi.org/10.5194/acp-21-5195-2021

Radenz, M., Bühl, J., Seifert, P., Baars, H., Engelmann, R., Barja González, B., et al. (2021). Hemispheric contrasts in ice formation in stratiform mixed-phase clouds: Disentangling the role of aerosol and dynamics with ground-based remote sensing. *Atmospheric Chemistry and Physics*, *21*(23), 17969–17994. https://doi.org/10.5194/acp-21-17969-2021

Radenz, M., Engelmann, R., Henning, S., Schmithüsen, H., Baars, H., Frey, M. M., et al. (2024). Ground-based remote sensing of aerosol, clouds, dynamics, and precipitation in Antarctica —first results from the one-year COALA campaign at Neumayer station III in 2023. *Bulletin of the American Meteorological Society*, *105*(8), E1438–E1457. https://doi.org/10.1175/BAMS-D-22-0285.1

Seifert, P., Ansmann, A., Mattis, I., Wandinger, U., Tesche, M., Engelmann, R., et al. (2010). Saharan dust and heterogeneous ice formation: Eleven years of cloud observations at a central European EARLINET site. *Journal of Geophysical Research*, *115*(D20), D20201. https://doi.org/10.1029/2009JD013222

Seifert, P., Ansmann, A., Müller, D., Wandinger, U., Althausen, D., Heymsfield, A. J., et al. (2007). Cirrus optical properties observed with lidar, radiosonde, and satellite over the tropical Indian Ocean during the aerosol-polluted northeast and clean maritime southwest monsoon. *Journal of Geophysical Research*, *112*(D17), D17205. https://doi.org/10.1029/2006JD008352

Sekelsky, S. M., Ecklund, W. L., Firda, J. M., Gage, K. S., & McIntosh, R. E. (1999). Particle size estimation in ice-phase clouds using multifrequency radar reflectivity measurements at 95, 33, and 2.8 GHz. *Journal of Applied Meteorology*, *38*(1), 5–28. https://doi.org/10.1175/1520-0450(1999)038⟨0005:PSEIIP⟩2.0.CO;2

Shen, H., Yin, Z., He, Y., Ansmann, A., Zhan, Y., Wang, L., & Jing, D. (2024). Impact of Asian dust on cirrus formation over the central Pacific: CALIOP- and cloudsat-observation-based case studies. *Journal of Geophysical Research: Atmospheres*, *129*(20), e2024JD041265. https://doi.org/10.1029/2024JD041265

Tan, I., Storelvmo, T., & Zelinka, M. D. (2016). Observational constraints on mixed-phase clouds imply higher climate sensitivity. *Science*, *352*(6282), 224–227. https://doi.org/10.1126/science.aad5300

Tesche, M., Ansmann, A., Müller, D., Althausen, D., Engelmann, R., Freudenthaler, V., & Groß, S. (2009). Vertically resolved separation of dust and smoke over Cape Verde using multiwavelength Raman and polarization lidars during Saharan mineral dust experiment 2008. *Journal of Geophysical Research*, *114*(D13), D13202. https://doi.org/10.1029/2009JD011862

Tobo, Y., Prenni, A. J., DeMott, P. J., Huffman, J. A., McCluskey, C. S., Tian, G., et al. (2013). Biological aerosol particles as a key determinant of ice nuclei populations in a forest ecosystem. *Journal of Geophysical Research: Atmospheres*, *118*(17), 10100–10110. https://doi.org/10.1002/jgrd.50801

Twohy, C. H., DeMott, P. J., Russell, L. M., Toohey, D. W., Rainwater, B., Geiss, R., et al. (2021). Cloud-nucleating particles over the Southern Ocean in a changing climate. *Earth's Future*, *9*(3), e2020EF001673. https://doi.org/10.1029/2020EF001673

Ulbrich, C. W. (1983). Natural variations in the analytical form of the raindrop size distribution. *Journal of Applied Meteorology and Climatology*, *22*(10), 1764–1775. https://doi.org/10.1175/1520-0450(1983)022⟨1764:NVITAF⟩2.0.CO;2

Vergara-Temprado, J., Miltenberger, A. K., Furtado, K., Grosvenor, D. P., Shipway, B. J., Hill, A. A., et al. (2018). Strong control of Southern Ocean cloud reflectivity by ice-nucleating particles. *Proceedings of the National Academy of Sciences*, *115*(11), 2687–2692. https://doi.org/10.1073/pnas.1721627115

Welti, A., Bigg, E. K., DeMott, P. J., Gong, X., Hartmann, M., Harvey, M., et al. (2020). Ship-based measurements of ice nuclei concentrations over the Arctic, Atlantic, Pacific and Southern oceans. *Atmospheric Chemistry and Physics*, *20*(23), 15191–15206. https://doi.org/10.5194/acp-20-15191-2020

Yang, X., Zhao, C., Yang, Y., Yan, X., & Fan, H. (2021). Statistical aerosol properties associated with fire events from 2002 to 2019 and a case analysis in 2019 over Australia. *Atmospheric Chemistry and Physics*, *21*(5), 3833–3853. https://doi.org/10.5194/acp-21-3833-2021

Yi, Y., Yi, F., Huang, K., Liu, F., Zhang, Y., Yu, C., et al. (2024). Locally formed thin supercooled liquid stratiform clouds on mid-level moisture advection layers as observed by ground-based lidars, radar, and radiosondes at a subtropical site. *Journal of Geophysical Research: Atmospheres*, *129*(22), e2024JD041405. https://doi.org/10.1029/2024JD041405

Zhang, D., Wang, Z., Kollias, P., Vogelmann, A. M., Yang, K., & Luo, T. (2018). Ice particle production in mid-level stratiform mixed-phase clouds observed with collocated A-Train measurements. *Atmospheric Chemistry and Physics*, *18*(6), 4317–4327. https://doi.org/10.5194/acp-18-4317-2018

Zhang, H., Zhao, C., Xia, Y., & Yang, Y. (2023). North Atlantic oscillation–associated variation in cloud phase and cloud radiative forcing over the Greenland ice sheet. *Journal of Climate*, *36*(10), 3203–3215. https://doi.org/10.1175/JCLI-D-22-0718.1

Zhao, L., Wang, Y., Zhao, C., Dong, X., & Yung, Y. L. (2022). Compensating errors in cloud radiative and physical properties over the Southern Ocean in the CMIP6 climate models. *Advances in Atmospheric Sciences*, *39*(12), 2156–2177. https://doi.org/10.1007/s00376-022-2036-z

Zhao, X., Liu, X., Burrows, S., DeMott, P. J., Diao, M., McFarquhar, G. M., et al. (2023). Important ice processes are missed by the community Earth system model in Southern Ocean mixed-phase clouds: Bridging SOCRATES observations to model developments. *Journal of Geophysical Research: Atmospheres*, *128*(4), e2022JD037513. https://doi.org/10.1029/2022JD037513